

## The effect of MFI zeolite lamellar and related mesostructures on toluene disproportionation and alkylation†

Cite this: *Catal. Sci. Technol.*, 2013, **3**, 2119

Changbum Jo,<sup>ab</sup> Ryong Ryoo,<sup>\*ab</sup> Naděžda Žilková,<sup>c</sup> Dana Vitvarová<sup>c</sup> and Jiří Čejka<sup>\*c</sup>

The effect of MFI zeolite nanosheet morphology and related mesostructures on the accessibility of acid sites evaluated from FTIR spectra of different adsorbed probe molecules and conversions and selectivities in toluene disproportionation and alkylation with isopropyl alcohol was investigated. Two-dimensional MFI lamellar zeolite (1.5 nm thickness of layers) and related mesoporous sponge morphologies, most probably with 10-ring channel system not yet structurally fully determined, were synthesized and characterized by XRD, SEM, TEM, and adsorption measurements. FTIR spectroscopy using pyridine, deuterated acetonitrile and 2,6-di-*tert*-butyl pyridine evidenced high concentrations of accessible Lewis acid sites at the expense of Brønsted acid sites. Ordered mesoporous zeolites exhibited slightly higher toluene conversion in its alkylation with isopropyl alcohol than lamellar MFI or conventional MFI due to easy access to active sites. The lamellar zeolite consisting of less than a unit cell layer was slightly more active than MFI but still exhibited high selectivity to *p*-cymene. It evidences that alkylation of toluene with isopropyl alcohol proceeds mainly in the 10-ring channel system of MFI zeolite, although the effect of large external surface cannot be neglected. Increased para-selectivity compared with thermodynamic value is achieved even in the case of extremely thin zeolite nanosheets.

Received 1st March 2013,  
Accepted 29th April 2013

DOI: 10.1039/c3cy00146f

[www.rsc.org/catalysis](http://www.rsc.org/catalysis)

### 1. Introduction

Zeolites are the most important heterogeneous catalysts possessing numerous large-scale industrial applications in refining, petrochemistry, environmental protection, and fine chemical synthesis.<sup>1–4</sup> The particular success of zeolites is due to their high thermal and hydrothermal stability, and optimum micropore systems affording shape-selectivity, controlled acidity and environmental tolerance.<sup>5–7</sup> Despite many applications and even more promising laboratory results, there is an on-going significant research effort to prepare new structural types of zeolites, to modify their properties by direct synthesis or post-synthesis manipulations, or to optimize the morphology of zeolite crystals for a particular application.<sup>8–10</sup>

Both chemical and textural properties of zeolites influence substantially the resulting activities/selectivities in various reactions. For several decades, zeolites were synthesized and considered as typical crystalline microporous materials with the edge dimensions of their crystals being rather similar or one of them being significantly smaller than the two remaining.<sup>11</sup> The crystal size together with the limited size of zeolite channel entrances restricts formation or transformations with bulky organic molecules being unable to penetrate into the channel system. In the case when shape-selectivity is not of high importance for the chemical reactions, external surface of zeolites can serve sufficiently as highly active catalyst. This can be achieved in principle in the following ways: (i) decreasing the size of zeolite crystals, (ii) forming mesopores inside the zeolite crystals, and (iii) forming zeolite layers exhibiting large external surface areas.

The first layered zeolite precursor MCM-22(P) was prepared by researchers at Mobil and the precursor was subsequently swollen and pillared creating MCM-36.<sup>12</sup> This was followed by rapid development in this area providing delaminated ITQ-2.<sup>13</sup> Recently, the delamination method was further developed to the preparation of various types of “two-dimensional” zeolites with the third dimension of size of about 1–2 unit cell parameters, such as MWW, SOD, FER and NSI.<sup>13–18</sup> On the other hand, Ryoo and co-workers

<sup>a</sup> Center for Nanomaterials and Chemical Reactions, Institute for Basic Science (IBS), Daejeon 305-701, Korea

<sup>b</sup> Department of Chemistry, KAIST, Daejeon 305-701, Korea.  
E-mail: ryongryoo@kaist.ac.kr

<sup>c</sup> J. Heyrovský Institute of Physical Chemistry, Academy of Sciences of the Czech Republic, v.v.i., Dolejškova 3, CZ-182 23 Prague 8, Czech Republic.  
E-mail: jiri.cejka@jh-inst.cas.cz

† Electronic supplementary information (ESI) available. See DOI: 10.1039/c3cy00146f

discovered a zeolite synthesis method using multi-ammonium surfactants functionalized with zeolite structure-directing agents (SDAs).<sup>19,20</sup> The surfactant molecules of this type form micelles functioning as SDA at a mesostructure level while the multiammonium head groups acted as SDAs for crystalline microporous zeolites. In this surfactant-directed synthesis route, the framework topologies MFI, MTW, BEA, and MRE were prepared and the thickness could be tailored by using surfactants with different head group structures.<sup>17,21,22</sup> For example, zeolite MFI with the framework thickness ranging from 1.5 to 3.5 nm could be synthesized using Gemini-type organic surfactants containing 3–5 ammonium groups.<sup>14</sup> Furthermore, it was possible to synthesize the nano-sponge-like zeolite as a network of short branched nanorods by modifying the overall surfactant structure.<sup>14</sup> Synthesis of two-dimensional zeolites can be assessed as an important breakthrough in the area of zeolite synthesis, as preparation of tiny zeolitic layers enables their further manipulation providing swollen, delaminated, or pillared materials and in some cases results in the preparation of real three-dimensional mesoporous structures.<sup>23–28</sup>

While conventional zeolites currently represent the most important industrial heterogeneous catalysts, the maximum pore size of zeolite applied industrially is still only 0.74 nm for zeolite FAU. Although many zeolites have been recently prepared with large pores, none of them are industrially applied yet. In contrast, layered zeolites (two-dimensional zeolites) show interesting catalytic properties, sometime being superior to conventional zeolites. When shape selective properties of zeolites are not required for the catalytic application, two-dimensional zeolites may be preferred.<sup>16</sup> Regarding that, Corma's group provided an interesting example of the formation of bulky 2-methyl-2-naphthyl-4-methyl-1,3-dioxolane.<sup>29</sup> The application of two-dimensional zeolites is not limited to acid catalyzed reactions.<sup>13,30</sup> In fact, introduction of Ti to ITQ-2 or ITQ-6 materials provided highly active epoxidation catalysts<sup>31,32</sup> and two-dimensional (delaminated) ITQ-6 served as a support for immobilization of enzymes.<sup>33</sup> Other examples of excellent catalytic activities of two-dimensional zeolites were reported in detail in ref. 16 and 18.

This contribution focuses on the characterization of novel two-dimensional zeolites, although the final structure of some of them is not yet determined. We compare here conventional MFI zeolite, mesoporous MCM-41 with two-dimensional MFI prepared using a specially designed template<sup>14</sup> and another two, most probably also 10-ring zeolites also present in two-dimensional form. These materials are characterized in detail by X-ray powder diffraction, sorption capacities, SEM, TEM, and FTIR spectroscopy using different probe molecules. Catalytic properties of all materials under study were evaluated based on toluene disproportionation and toluene alkylation with isopropyl alcohol. The main attention was paid not only to toluene conversions in both reactions but also different selectivities to understand in detail the role of the chemical and textural parameters.

## 2. Experimental

### 2.1. Synthesis of zeolite

Zeolite samples, exhibiting two-dimensional crystal morphologies or their assemblage into three-dimensionally mesoporous

structure, were hydrothermally synthesized using Gemini-type multi-quaternary ammonium surfactants having formulas  $[C_{18}H_{37}N^+(Me)_2\{C_6H_{12}N^+(Me)_2\}_{n-2}C_6H_{12}N^+(Me)_2C_{18}H_{37}][Br^-]_n$  ( $n = 3, 4$  and  $5$ ) as zeolite structure-directing agents (SDAs). The surfactants are denoted as '18-N<sub>n</sub>-18' for brevity. These surfactants were synthesized in the laboratory as described elsewhere.<sup>34</sup> The starting gel composition was 30 SiO<sub>2</sub>:0.5 Al<sub>2</sub>O<sub>3</sub>:*a* 18-N<sub>n</sub>-18:6.6 Na<sub>2</sub>O:1070 H<sub>2</sub>O, where *a* was varied from 1.3 to 0.8 to fix the ratio of SiO<sub>2</sub>/N<sup>+</sup> at 7.5. To prepare the initial synthesis gel, the bromide form of 18-N<sub>n</sub>-18 was dissolved in distilled water containing sodium hydroxide and sodium aluminate (Aldrich, 42.5% Al<sub>2</sub>O<sub>3</sub>, 53% Na<sub>2</sub>O). Tetraorthosilicate (Junsei, 98%) was added at once into a polypropylene bottle containing this solution. The bottle was immediately shaken vigorously by hand. After further mixing using a mechanical stirrer for 6 h in an oven at 60 °C, the resultant gel was transferred into a Teflon-lined stainless steel autoclave. The autoclave was tumbled with mixing baffles at 60 rpm in an oven at 140 °C. When 18-N<sub>3</sub>-18 was used as a zeolite SDA, the precipitated solid was sampled at 1, 5 and 9 d periods of hydrothermal reaction time. In the case of 18-N<sub>4</sub>-18 and 18-N<sub>5</sub>-18, the precipitated solids were collected at 5 d. The collected samples were filtered, washed with distilled water, dried at 100 °C, and finally calcined in air at 580 °C. The calcined samples were treated twice for ammonium exchange, using a 1 M aqueous solution of NH<sub>4</sub>Cl at room temperature followed by profound washing in distilled water. The NH<sub>4</sub><sup>+</sup> ion-exchanged samples were then calcined at 550 °C to convert to the H<sup>+</sup> ionic form.

For comparison, MFI zeolite purchased from Zeolyst (Si/Al = 35) was used. This zeolite was ion-exchanged with ammonium nitrate (four times) followed by filtration, washed out with distilled water, dried and calcined at 450 °C for 20 h.

The following samples were investigated:

N<sub>3</sub>-1d: hexagonal mesostructure, amorphous frameworks like MCM-41

N<sub>3</sub>-5d: ordered hexagonal mesostructure, 10-ring zeolite

N<sub>3</sub>-9d: 1.5 nm thick MFI nanosheet, 2 pentasil layers

N<sub>4</sub>-5d: disordered mesostructure, 10-ring zeolite of 2.1 nm thickness

N<sub>5</sub>-5d: disordered mesostructure, 10-ring zeolite of 2.7 nm thickness

MFI: conventional zeolite (Zeolyst)

### 2.2. Preparation of carbon replicas of disordered mesostructure zeolites

To synthesize carbon replicas of N<sub>4</sub>-5d and N<sub>5</sub>-5d, the 0.1 g of N<sub>4</sub>-5d and N<sub>5</sub>-5d samples were impregnated with an aqueous solution of sucrose (0.13 g) and sulfuric acid (0.08 ml). The resultant mixture was dried at 100 °C for 6 h in a drying oven, and subsequently dried at 140 °C for 6 h to remove remaining water. After heating, the carbon/mesostructured zeolite composite were impregnated again with 65% of the amount of the first aforementioned mixture. After heating to 160 °C again, the black powder was further heated to 450 °C for 3 h and maintained for 1 h. Subsequently, the temperature increased further

to 700 °C for 2 h and placed for 4 h using a quartz tube. The aluminosilicates framework in the resultant carbon/mesostructured zeolite composite was removed by successive washing with HF solution.

### 2.3. Zeolite characterization

XRD patterns were recorded with a Rigaku Multiflex diffractometer using Cu K $\alpha$  radiation ( $\lambda = 0.1541$  nm) at 30 kV and 40 mA.

Nitrogen adsorption–desorption isotherms were measured with a Micromeritics Tristar II volumetric adsorption analyzer at  $-196$  °C after degassing the H<sup>+</sup> form of samples for 6 h at 300 °C. The specific surface area was calculated from the adsorption branch in the range of  $0.1 \leq P/P_0 \leq 0.3$  using the Brunauer–Emmett–Teller (BET) equation. The pore size distribution was estimated using the Barrett–Joyner–Halenda (BJH) algorithm. Ar adsorption–desorption isotherms were measured with Micromeritics ASAP 2020 at  $-186$  °C. Micropore size distribution was estimated by using the Non-Localized Density Functional Theory (NLDFT) calculation from the adsorption branch of Ar isotherm. TEM images were obtained by a Philips F30 Tecnai with accelerating voltage of 300 kV. SEM images were taken using a Hitachi S-4800 without a metal coating. <sup>27</sup>Al magic angle spinning NMR spectra were recorded on a Bruker Avance 400 NMR spectrometer operated at 104.27 MHz. All spectra were obtained under the following conditions: 14 kHz spinning rate, 2.5  $\mu$ s pulse and 0.5 s relaxation delay.

### 2.4. Characterization of acidity

The concentration and type of acid sites were determined by adsorption of CD<sub>3</sub>CN, pyridine (py) and di-*tert*-butylpyridine (DTBpy) as probe molecules followed by FTIR spectroscopy (Nicolet 6700 FTIR with AEM module). Prior to the adsorption, self-supporting wafers of individual catalysts were activated *in situ* by overnight evacuation at temperature 450 °C.

Adsorption of CD<sub>3</sub>CN was studied on a Nicolet 6700 AEM module equipped with DTGS detector. CD<sub>3</sub>CN adsorption proceeded at room temperature for 30 min at equilibrium pressure 5 Torr, followed by 30 min degassing at room temperature. To obtain a quantitative analysis, molar absorption coefficients for CD<sub>3</sub>CN adsorbed on Brønsted acid sites ( $\nu(\text{C}\equiv\text{N})\text{-B}$  at 2297 cm<sup>-1</sup>,  $\epsilon(\text{B}) = 2.05 \pm 0.1$  cm  $\mu\text{mol}^{-1}$ ) and strong and weak Lewis acid sites ( $\nu(\text{C}\equiv\text{N})\text{-L1}$  at 2325 cm<sup>-1</sup>,  $\nu(\text{CN})\text{-L2}$  at 2310 cm<sup>-1</sup>,  $\epsilon(\text{L}) = 3.6 \pm 0.2$  cm  $\mu\text{mol}^{-1}$ ) were used. Integral intensities of individual bands were used and spectra were normalized to the wafer thickness, 10 mg cm<sup>-2</sup>.

Adsorption of pyridine was investigated on a Nicolet 6700 spectrometer equipped with MCT detector. Pyridine adsorption proceeded at 150 °C for 20 min at partial pressure 3 Torr, followed by 20 min evacuation at different temperatures (150 °C, 250 °C, 350 °C, 450 °C). The concentrations of Brønsted and Lewis acid sites were calculated from integral intensities of individual bands characteristic of pyridine on Brønsted acid sites at 1545 cm<sup>-1</sup> and the band of pyridine on Lewis acid site at 1455 cm<sup>-1</sup> and molar absorption coefficients of  $\epsilon(\text{B}) = 1.67 \pm 0.1$  cm  $\mu\text{mol}^{-1}$  and  $\epsilon(\text{L}) = 2.22 \pm 0.1$  cm  $\mu\text{mol}^{-1}$ , respectively.

The spectra were recorded with a resolution of 2 cm<sup>-1</sup> by collection of 128 scans for a single spectrum.

Adsorption of DTBpy was studied on a Nicolet 6700 AEM module equipped with a DTGS detector. DTBpy adsorption proceeded at 150 °C for 15 min at equilibrium pressure 0.8 Torr, followed by 1 h degassing at the same temperature. The concentration of Brønsted acid sites was calculated from integral intensity of the band characteristic of DTBpy on Brønsted acid sites at 1530 cm<sup>-1</sup> and molar absorption coefficient of  $\epsilon(\text{B}) = 1.67 \pm 0.1$  cm  $\mu\text{mol}^{-1}$ .

### 2.5. Catalytic reactions

Toluene disproportionation and alkylation with isopropyl alcohol were investigated in the gas phase under atmospheric pressure using a glass fixed-bed microreactor. Each catalyst was pressed into the pellets, crushed and sieved to obtain particles with a diameter in the range of 0.50–0.71 mm. Prior to the reaction, a given amount of the catalyst was activated *in situ* at 500 °C for 120 min in a stream of nitrogen (40 ml min<sup>-1</sup>), and then the activated catalyst was cooled down to the preset reaction temperature. In the case of toluene disproportionation the reaction temperature was 450 and 500 °C, weight hourly space velocity (WHSV) 2 and 20 h<sup>-1</sup>, and the concentration of toluene in the stream was 18.5 mol%. Toluene alkylation was studied at the reaction temperatures 200 and 250 °C. The WHSV related to toluene was 10 h<sup>-1</sup>, the concentration of toluene was 18.5 mol%, and toluene to isopropyl alcohol molar ratio was 9.6.

The reaction mixtures were analyzed using an on-line gas chromatograph (HP 6890) equipped with an FID detector and a capillary column (DB-5, 50 m  $\times$  0.32 mm  $\times$  1  $\mu$ m) in toluene alkylation, while HP-INNOWax column (30 m  $\times$  0.32 mm  $\times$  0.5  $\mu$ m) was used for toluene disproportionation studies. The first sample was taken after 15 min of time-on-stream (T-O-S) and the other samples were taken at the interval of 60 min.

## 3. Results and discussion

Fig. 1 shows the XRD patterns and TEM images of the hydrothermal reaction products synthesized with 18-N<sub>3</sub>-18, which were converted to the H<sup>+</sup>-form. As shown in the XRD patterns, the product collected after 1 d of hydrothermal reaction exhibited three sharp XRD peaks centered at 1.9, 3.2 and 3.8° 2 $\theta$ . This result indicates that the product was a mesoporous aluminosilicate material with hexagonal structure similar to MCM-41. The mesopore walls were built with amorphous frameworks as indicated by the absence of XRD peak in wide-angle region (*i.e.*, 5° < 2 $\theta$  < 40°). The MCM-41-like low-angle XRD feature was completely lost when the sample was converted to the H<sup>+</sup>-ionic form *via* NH<sub>4</sub><sup>+</sup> exchange. This sample in the H<sup>+</sup>-form is denoted by N<sub>3</sub>-1d, meaning for the reaction time with 18-N<sub>3</sub>-18 for 1 d. Similarly, the other products collected at 5 and 9 d and subsequently converted to the H<sup>+</sup>-ionic form are denoted by N<sub>3</sub>-5d and N<sub>3</sub>-9d, respectively. After the ion exchange treatment, the Na content of N<sub>3</sub>-5d and N<sub>3</sub>-9d became undetectable with inductively coupled plasma (ICP) analysis. In the case of N<sub>3</sub>-1d, however, the Na content amounted to 3.85 Na/Al. The high Na

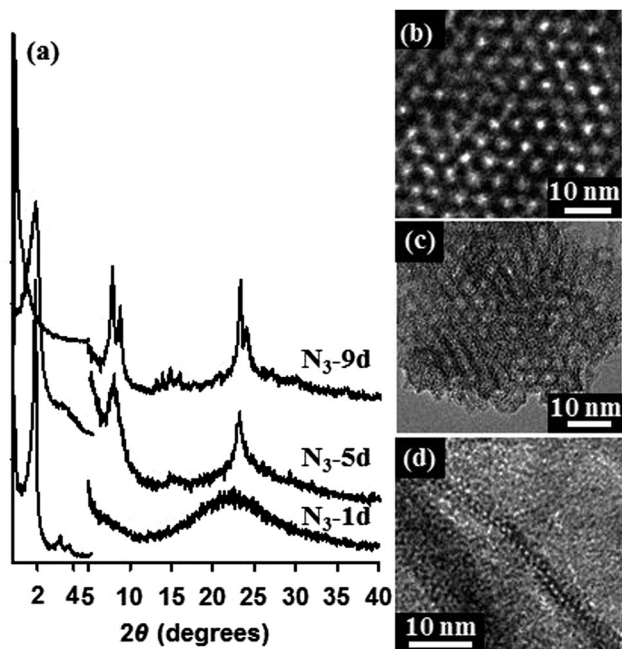


**Fig. 1** XRD patterns (a) and their corresponding TEM images of (b)  $N_3$ -1d (before  $NH_4^+$  ion-exchange) (c)  $N_3$ -5d and (d)  $N_3$ -9d.

content of  $N_3$ -1d could be due to the Na occlusion when the porous structure collapsed during the attempt for ion exchange. Adsorption isotherms and pore size distributions of lamellar and mesostructured samples under study are given in the ESI† (Fig. S1–S4).

In the case of the  $N_3$ -5d product, the XRD pattern also shows three well-resolved reflections at the low-angle region. These XRD peaks could be indexed to a hexagonal mesostructure with  $d_{10} \approx 4.3$  nm, which indicated that the sample still possesses a hexagonal-type mesostructure similar to the case of  $N_3$ -1d. However, a close examination of the XRD data revealed that each of the XRD peak positions was shifted to the lower-angle side as compared with  $N_3$ -1d. That indicates an expansion of the hexagonal lattice during the reaction period between 1 and 5 d. The hydrothermal synthesis for 5 d was identical to the previous synthesis of hexagonally ordered mesoporous MFI zeolite, except for the present Si/Al ratio of 30 as compared to 20 in the previous work.<sup>14</sup> The product collected at 5 d had the same structure and morphology as the hexagonal mesoporous MFI-like zeolite. A high-resolution TEM investigation of the  $N_3$ -5d sample evidences that the original mesopore walls were

converted to a crystalline microporous zeolitic structure during this hydrothermal reaction period (Fig. 1c, Fig. S5, ESI†). In agreement with the crystalline structure, new XRD peaks appeared at 7.9, 15.2 and 22.8° in the high-angle XRD region of the  $N_3$ -5d sample. These diffraction lines were rather broad, indicating that the mesopore walls were composed of tiny pieces of crystalline domains. The framework structure of the mesopore walls were difficult to determine accurately due to the severe line broadening and insufficient number of reflections. This material exhibits a type-IV argon adsorption isotherm with a hysteresis loop about  $P/P_0 = 0.45$  due to a capillary condensation in mesopore. The adsorption isotherm also exhibited a very sharp increase in the adsorption amount with increasing pressure in the region of  $0 < P/P_0 < 0.1$ . The resulting pore-size distribution showed a very sharp peak centered at 0.55 nm, and another broad peak at 3.3 nm (Fig. S1, ESI†). The pore diameter of 0.55 nm could be described as a kind of micropore corresponding to 10-ring apertures in the zeolite framework. The larger pores could be explained by the formation of mesopores, of which the walls were composed of the 0.55 nm microporous zeolitic frameworks.

When the hydrothermal reaction time was prolonged to 9 d, the resultant product,  $N_3$ -9d, exhibited no low-angle reflections. On the other hand, the high-angle XRD peaks were better resolved than those of  $N_3$ -9d. The high-angle XRD peaks well match to the (*h*0*l*) reflections corresponding to the MFI zeolite structure, except for the absence of the reflections along the *b*-axis direction (Fig. 1a). The absence of these reflections indicates that the zeolite morphology could be extremely thin in this direction. The TEM image of Fig. 1d confirmed that the sample has morphology of MFI zeolite in the form of 2-dimensional nanosheets (Fig. S6, ESI†). Each nanosheet is composed of a single layer of micropores, and accordingly, has a 1.5 nm thickness. This thickness was corresponding to 3/4 of the *b* lattice parameter ( $b = 1.97$  nm) of the MFI framework topology. Thus, the solid precipitates collected at 9 d was a 2-dimensional nanomorphous MFI zeolite, of which the thickness was less than a unit-cell dimension of MFI zeolite along the *b*-axis. The zeolite nanosheets were assembled in a disordered manner. This zeolite sample does not exhibit low-angle XRD diffraction lines because of significant disordered arrangement of the nanosheets. Despite the disordered assembly, the nanosheets retain mesopores with remarkably uniform diameters between adjacent nanosheets. The textural properties of the  $N_3$ -9d zeolite sample and also those of the aforementioned  $N_3$ -1d and  $N_3$ -5d samples are summarized in Table 1.

**Table 1** Textural properties of  $N_3$ -1d,  $N_3$ -5d,  $N_3$ -9d,  $N_4$ -5d and  $N_5$ -5d

Sample	Mesophase	Mean micropore diameter (nm)	Mean mesopore diameter (nm)	BET surface area ( $m^2 g^{-1}$ ) (external surface area) <sup>b</sup>	Pore volume ( $ml g^{-1}$ )	Wall thickness (nm)
$N_3$ -1d	Hexagonal	n.d. <sup>a</sup>	2.4	221 (220)	0.16	1.5 <sup>c</sup>
$N_3$ -5d	Hexagonal	0.55	3.3	1090 (990)	1.40	1.7 <sup>c</sup>
$N_3$ -9d	Nanosheet	0.55	3.0	693 (555)	1.01	1.5 <sup>d</sup>
$N_4$ -5d	Disordered	0.55	3.4	970 (805)	1.52	2.1
$N_5$ -5d	Disordered	0.55	5.1	810 (622)	1.53	2.7

<sup>a</sup> Not defined. <sup>b</sup> External surface area was evaluated from the *t*-plot method. <sup>c</sup> Wall thickness was determined from the mesopore diameter and the hexagonal lattice parameter analyzed by XRD. <sup>d</sup> Wall thickness was measured from the TEM image.

Fig. 2 shows the XRD patterns and TEM images of the products synthesized using 18-N<sub>4</sub>-18 and 18-N<sub>5</sub>-18 as SDAs. The samples were collected after 5 d hydrothermal reaction, and subsequently converted to the H<sup>+</sup>-form. These samples are denoted by N<sub>4</sub>-5d and N<sub>5</sub>-5d, respectively. Similar to the aforementioned cases of N<sub>3</sub>-5d and N<sub>3</sub>-9d, the Na content of N<sub>4</sub>-5d, N<sub>5</sub>-5d and conventional MFI decreased to an undetectable level by the ion exchange treatment. As shown in the XRD pattern, both N<sub>4</sub>-5d and N<sub>5</sub>-5d exhibit three broad diffraction lines centered at 7.9, 15.2 and 22.8° 2θ, in the wide-angle region. The high-angle XRD patterns were very similar to the N<sub>3</sub>-5d sample (Fig. 2a). The samples exhibited very similar argon adsorption isotherms to N<sub>3</sub>-5d. We expect that N<sub>4</sub>-5d and N<sub>5</sub>-5d possess a 10-ring microporous framework similar to the sample N<sub>3</sub>-5d. The exact framework structures of N<sub>4</sub>-5d and N<sub>5</sub>-5d were difficult to determine. The TEM images in Fig. 2b and c show that thin layers of zeolitic frameworks were interconnected in a disordered manner (Fig. S7 and S8, ESI†). The 3-dimensional network, which was reminiscent of a nanosponge, retained a large volume of mesopores. The mesopore size distribution (analyzed using nitrogen adsorption) exhibited a very sharp peak centered at 3.4 nm for N<sub>4</sub>-5d and 5.1 nm for N<sub>5</sub>-5d, indicating that the mesopore diameters were quite uniform. Despite their apparently disordered arrangement of mesopores, the nanosponge-like structure had a short-range structural correlation between the nearest mesopore walls (*i.e.*, zeolite layers). The low-angle peak in Fig. 2a indicates the short range structural order (1.4° 2θ for N<sub>4</sub>-5d, and 1.3° 2θ for N<sub>5</sub>-5d). The low-angle peak for N<sub>5</sub>-5d appeared at 2θ = 1.3° as a shoulder (arrow in Fig. 2a) on the background scattering, as opposed to a very sharp peak in the case of N<sub>4</sub>-5d. The less distinct XRD peak for N<sub>5</sub>-5d is attributed to the thicker walls of the mesopores, and lower structural coherence of the walls. The thickness of the mesopore walls could be determined by a method using carbon replication (Fig. S9, ESI†). The carbon replica exhibited a very sharp distribution of pore size which

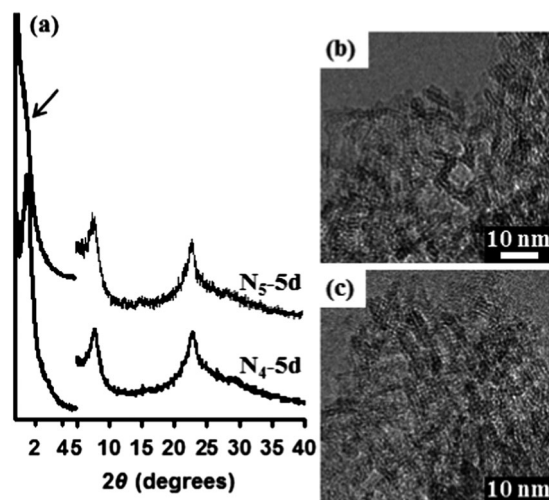


Fig. 2 XRD patterns (a) and their corresponding TEM images of (b) N<sub>4</sub>-5d and (c) N<sub>5</sub>-5d.

was centered at 2.1 nm in the case of N<sub>4</sub>-5d. The peak position increased to 2.7 nm in the case of N<sub>5</sub>-5d. These data correspond to the thicknesses of the zeolite layers and indicate that the zeolite framework thicknesses were quite uniformly tailored by the zeolite SDA surfactants. The framework thickness increased according to the number of ammonium groups in the surfactant. The textural properties of N<sub>4</sub>-5d and N<sub>5</sub>-5d are summarized in Table 1.

To characterize in detail the coordination and acidic properties of zeolitic materials under study, <sup>27</sup>Al MAS NMR and FTIR spectroscopy combined with adsorption of different probe molecules were employed. Fig. 3 presents the <sup>27</sup>Al MAS NMR spectra of lamellar and mesostructured materials under study. While spectra of samples N<sub>3</sub>-1d and N<sub>5</sub>-5d exhibit only tetrahedrally coordinated Al, the remaining samples contain in addition also less than 10% of octahedrally coordinated aluminum. This is in good agreement with FTIR spectra of hydroxyl regions not showing any Al–OH vibrations related to the presence of extra-framework aluminum species (Fig. 4).

FTIR spectroscopy was used to evaluate the type and concentrations of individual acid sites in two-dimensional zeolites and related materials. Fig. 4 shows the FTIR spectra of the area of

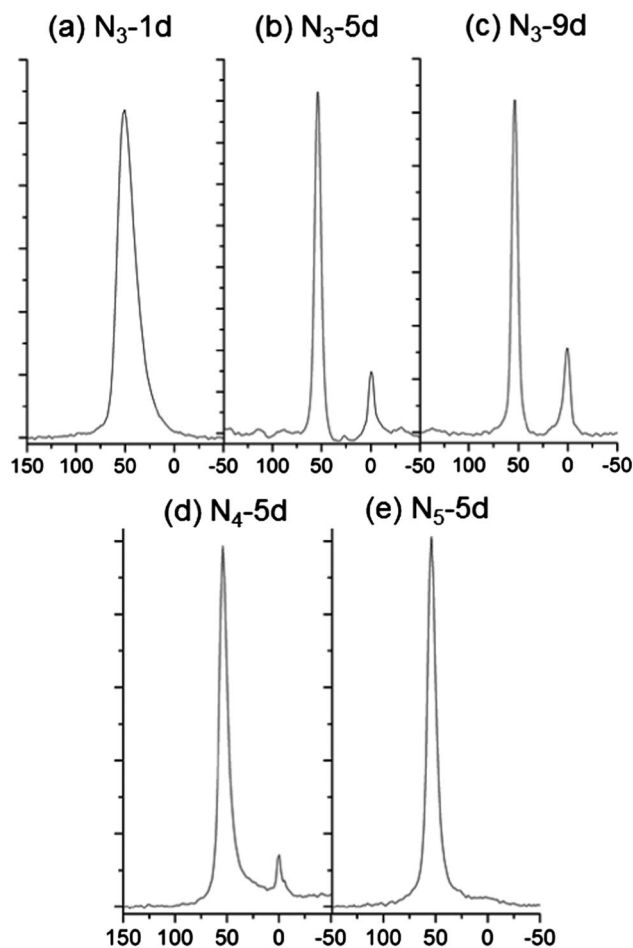
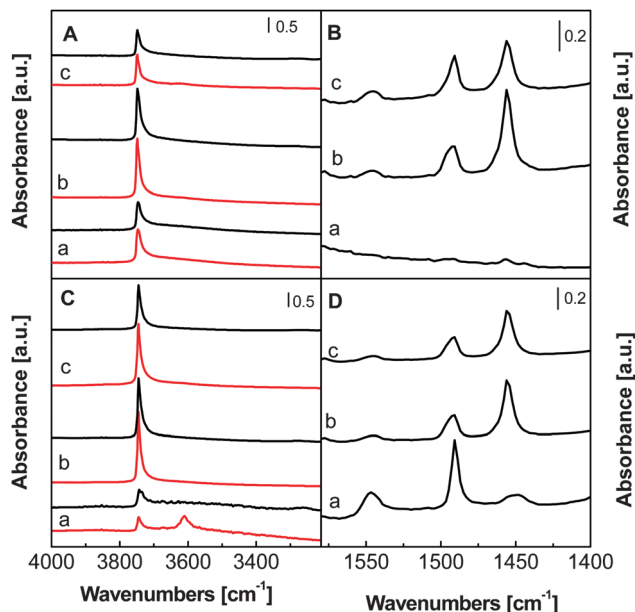


Fig. 3 <sup>27</sup>Al MAS NMR spectra of (a) N<sub>3</sub>-1d, (b) N<sub>3</sub>-5d, (c) N<sub>3</sub>-9d, (d) N<sub>4</sub>-5d, (e) and N<sub>5</sub>-5d. The <sup>27</sup>Al NMR spectra show tetrahedral Al (50–60 ppm) and octahedral Al (~0 ppm) sites.



**Fig. 4** IR spectra in the OH stretching region (A and C) and spectra of pyridine region after its adsorption (B and D) – A and B: (a) N<sub>3</sub>-1d, (b) N<sub>3</sub>-5d, (c) N<sub>3</sub>-9d; C and D: (a) MFI (b) N<sub>4</sub>-5d (c) N<sub>5</sub>-5d; for A and C: red line: spectra of activated samples, black line: spectra after 20 minutes desorption at 150 °C.

vibrations of hydroxyl groups and the area of vibrations of adsorbed pyridine. With the exception of zeolite MFI, all other materials show practically only one absorption band at about 3745 cm<sup>-1</sup> belonging to silanol groups. The characteristic absorption band of Si-OH-Al of acidic bridging OH groups is visible in the spectrum of MFI zeolite before adsorption of pyridine. However, after pyridine adsorption-desorption carried out at 150 °C, in the spectra of all samples with exception of MCM-41 one can see an absorption band at 1545 cm<sup>-1</sup>, which is typical of pyridine interacting with Brønsted acid sites. Thus, although the absorption bands of acidic OH groups are practically invisible, these materials possess distinct concentrations of Brønsted sites (Table 2). In contrast, concentration of Lewis acid sites (absorption band of pyridine around 1455 cm<sup>-1</sup>) is much higher as it is evidenced by a significantly higher intensity of the related absorption band. This fact can be explained in terms of the “two-dimensional” structure of these zeolites. It can be expected that such a morphological type of zeolite exhibits a higher concentration of defects from imperfectly grown zeolite crystals.

Different development of acidity is clearly visible from desorption of pyridine carried out at different temperatures. MCM-41 shows no Brønsted acid sites and only a small amount of Lewis acid sites. In all zeolite-based samples the concentration of Brønsted acid sites is always lower when compared with the concentration of Lewis acid sites. In addition, the concentration of Brønsted acid sites interacting with pyridine at higher desorption temperatures substantially decreases. This evidences a higher acid strength of most of Lewis acid sites when compared with Brønsted acid sites. It can be inferred that two-dimensional zeolites possess mainly Lewis sites due to the missing connectivities in the third dimension of the structure.

Important information arises from Tables 2 and 3. Concentrations of Brønsted as well as Lewis acid sites obtained from adsorption of pyridine are in good agreement with the data of adsorption of d<sub>3</sub>-acetonitrile, although they differ substantially in the size and basicity. It indicates that all acid sites are similarly accessible and that there are no “hidden” sites in these zeolitic materials. Adsorption of 2,6-di-*tert*-butyl pyridine proceeds exclusively on the external surface of zeolites despite their textural properties.<sup>35</sup> 2,6-Di-*tert*-butyl pyridine can also interact with some silanol groups. Based on the concentrations of 2,6-di-*tert*-butyl pyridine interacting with Brønsted acid sites, one can expect that most of Brønsted acid sites are located on the surface of two-dimensional zeolites and thus, they are easily accessible for bulky substrate molecules.

Toluene disproportionation and alkylation with isopropyl alcohol are important reactions both industrially as well as fundamentally. While toluene conversion in toluene disproportionation is mostly related to the number of acid sites and their accessibility,<sup>36,37</sup> in the case of toluene alkylation, the rate determining step of the reaction is desorption/transport of products.<sup>38</sup> In addition both reactions provide *para*-selective products of different sizes and thus, different diffusion coefficients.

Toluene disproportionation was carried out at 450 °C with WHSV = 20 h<sup>-1</sup> and 500 °C and 2 h<sup>-1</sup> (Fig. 5 and 6). Under both reaction conditions used, the conversions over catalysts studied provide the same order: MFI > disordered mesostructured 10-ring zeolites > hexagonally mesostructured 10-ring zeolite ~ two-dimensional MFI > MCM-41. The increase in the reaction temperatures from 450 to 500 °C led to an increase in the conversion of about one order of magnitude. Negligible conversion was achieved over MCM-41 indicating the decisive absence of Brønsted acid sites for toluene disproportionation. Higher conversions achieved with disordered mesostructured 10-ring zeolites in comparison with hexagonally mesostructured 10-ring zeolite and two-dimensional MFI indicate a higher accessibility of active sites in the case of two-dimensional MFI and hexagonally mesostructured 10-ring zeolite.

No significant differences were observed for selectivities or *para*-selectivity in xylenes under both reaction conditions. Selectivity to total xylenes are slightly less than 50% indicating that dealkylation proceeds at a limiting extent. With regard to that, the molar ratio of xylenes/benzene at 450 °C is between 0.90–0.95 and this value decreases to 0.85–0.90 at 500 °C evidencing an increasing rate of dealkylation reactions. Practically, no *para*-selectivity was achieved under both reactions. Concentrations of *p*-xylene were close to 30% at the reaction temperature of 450 °C while around 24% (thermodynamic value) at 500 °C.

When relating the acidic properties of zeolites under study (based on pyridine desorption at different temperatures and 2,6 DTBP adsorption, *cf.* Table 2 and Fig. 5 and 6) to catalytic activities in toluene disproportionation, it seems that the overall concentration of Brønsted acid sites is the dominating factor. Both lamellar and conventional MFI exhibit Brønsted acid sites of the highest strength among studied catalysts. Some of them still

**Table 2** Lewis (L) and Brønsted (B) acid site concentrations measured by pyridine adsorption after desorption in the range of 150–450 °C

Sample	Si/Al	Desorption temp (°C)	<i>c</i> (L) (mmol g <sup>-1</sup> )	<i>c</i> (B) (mmol g <sup>-1</sup> )	Sample	Si/Al	Desorption temp (°C)	<i>c</i> (L) (mmol g <sup>-1</sup> )	<i>c</i> (B) (mmol g <sup>-1</sup> )
N <sub>3</sub> -1d	20.2	150	0.007	0	N <sub>4</sub> -5d	28.2	150	0.261	0.048
		250	0.010	0			250	0.159	0.031
		350	0.013	0			350	0.122	0.014
		450	n.a.	n.a.			450	0.059	0
N <sub>3</sub> -5d	30.2	150	0.252	0.030	N <sub>5</sub> -5d	27.3	150	0.269	0.050
		250	0.165	0.022			250	0.264	0.048
		350	0.113	0.013			350	0.205	0.022
		450	0.053	0.006			450	0.059	0
N <sub>3</sub> -9d	38.4	150	0.176	0.072	MFI	54.9	150	0.070	0.158
		250	0.119	0.063			250	0.027	0.158
		350	0.067	0.044			350	0.020	0.144
		450	0.049	0.012			450	0.019	0.078

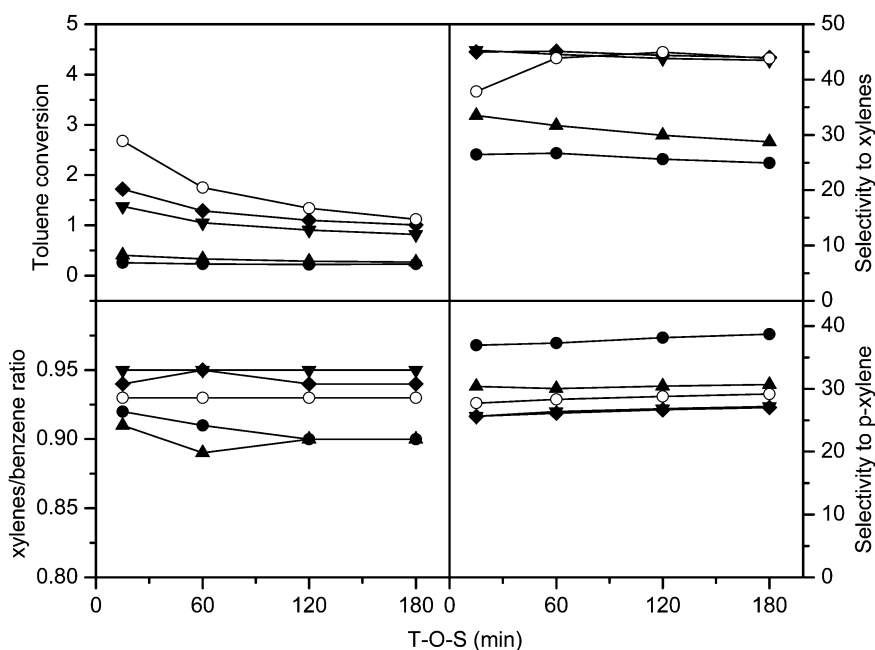
**Table 3** Lewis (L) and Brønsted (B) acid site concentrations measured by d<sub>3</sub>-acetonitrile adsorption and Brønsted (B) sites concentrations measured by 2,6-di-*tert*-butyl pyridine adsorption

Sample	Si/Al	CD <sub>3</sub> CN		2,6-DTBP <i>c</i> (B) (mmol g <sup>-1</sup> )
		<i>c</i> (L) (mmol g <sup>-1</sup> )	<i>c</i> (B) (mmol g <sup>-1</sup> )	
N <sub>3</sub> -1d	20.2	0.054	0	0.008
N <sub>3</sub> -5d	28.0	0.277	0.021	0.068
N <sub>3</sub> -9d	30.1	0.214	0.094	0.028
N <sub>4</sub> -5d	27.6	0.292	0	0.067
N <sub>5</sub> -5d	31.7	0.255	0	0.066

interact with pyridine even after desorption at 450 °C, which means at the reaction temperature. Thus, it looks that the strength of Brønsted acid sites is critical when comparing different lamellar, mesostructured and conventional 10-ring zeolites.

Toluene alkylation with isopropyl alcohol provides cymenes (isopropyltoluenes) as primary products. The reaction mechanisms of benzene or toluene alkylation from the structural point of view of used zeolites<sup>39</sup> as well as from the industrial standpoints<sup>40</sup> have been discussed in the literature. Depending on the structure, acidity and reaction conditions toluene (being in excess in the reaction mixture) can disproportionate to benzene and xylenes. In addition, a structurally very sensitive consecutive reaction is transalkylation between primarily formed cymene and toluene to *n*-propylbenzene. *n*-Propylbenzene is an undesired product but it evidences special features of the void reaction volume available in zeolites, particularly in channel intersections.<sup>41</sup>

Fig. 7 and 8 clearly show significant differences among individual zeolite catalysts tested at different reaction temperatures.

**Fig. 5** Toluene disproportionation over different nanostructured zeolite catalysts at 450 °C (● N<sub>3</sub>-5d (hexagonally mesostructure 10-ring zeolite), ▲ N<sub>3</sub>-9d (1.4 nm MFI nanosheet, 2 pentasil layers), ▼ N<sub>4</sub>-5d (disordered mesostructure 10-ring zeolite with 2.1 nm thickness), ◆ N<sub>5</sub>-5d (disordered mesostructure 10-ring zeolite with 2.7 nm thickness), MFI).

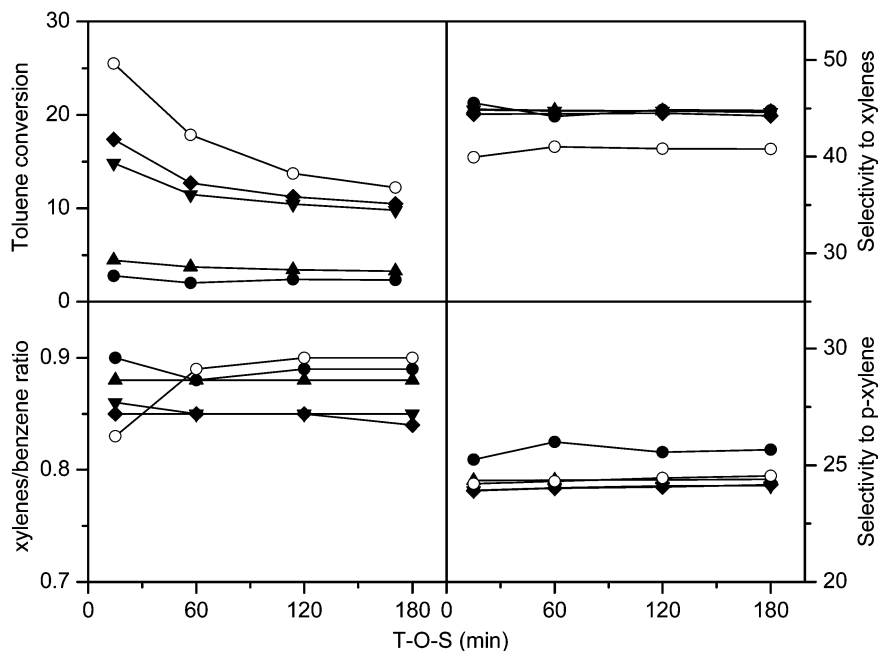


**Fig. 6** Toluene disproportionation over different nanostructured zeolite catalysts at 500 °C (● N<sub>3</sub>-5d (hexagonally mesostructure 10-ring zeolite), ▲ N<sub>3</sub>-9d (1.4 nm MFI nanosheet, 2 pentasil layers), ▼ N<sub>4</sub>-5d (disordered mesostructure 10-ring zeolite with 2.1 nm thickness), ◆ N<sub>5</sub>-5d (disordered mesostructure 10-ring zeolite with 2.7 nm thickness), MFI).

MCM-41 is practically inactive, therefore, selectivities to the individual products are extremely influenced by this negligible conversion. *n*-Propyltoluenes are practically not formed, which results in the *iso/n*-propyltoluene ratio being equal almost to infinity.

For comparison with other two-dimensional zeolites, including MFI, conventional MFI with Si/Al ratio 37 was used. All zeolite-based catalysts with 10-ring pore systems exhibited higher toluene conversion than conventional MFI. It should be noted that a significant excess of toluene in the reaction mixture (9.6 : 1) is used to prevent fast deactivation of the catalysts. Layered MFI having 1.4 nm nanosheets formed just by two pentasil layers exhibited slightly higher conversion than MFI. It indicates that these textural properties play a critical role in the alkylation reaction and the possibility of the reaction on the external surface of MFI layers or diffusion pathways inside the structure consisting of two pentasil layers do not slow down the rate of the alkylation reaction. Hexagonally mesostructured zeolite with a 10-ring channel system and two recently synthesized disordered mesostructured 10-ring zeolites differing in the thickness of their layers provide similar conversion in the range 7.0–7.5%.

Selectivity to cymenes is substantially influenced by the available reaction void volume in the zeolite channel system and it increases with the absence of 10-ring intersecting channels of MFI or MEL types required for the bimolecular formation of *n*-propyltoluenes. Žilková *et al.*<sup>42</sup> and Ivanova and coworkers<sup>43</sup> clearly evidenced that this bimolecular transformation involving transfer of propyl group from one benzene ring to another is connected with isomerization of an isopropyl group to an *n*-propyl group. This is the main reason for relatively low selectivity to cymenes over conventional MFI zeolite (60%). In contrast, layered MFI catalysts formed just by two-pentasil layers provided selectivity to cymenes of 75–80%. It strongly

evidences that the alkylation reaction has to proceed to a large extent inside these layers, as a significant amount of *n*-propyltoluenes is still formed. In the case of the other three zeolite-based catalysts selectivities to cymenes are higher than 90%. One should expect that pores of these zeolites are larger (although still 10-rings) than those of MFI or do not possess optimum channel intersections required for the formation of the bimolecular intermediate.<sup>28</sup> No *n*-propylbenzene was reported for cumene synthesis over nanomorphous zeolites BEA, MTW and MRE, which do not provide optimum channel intersections for running bimolecular formation of *n*-propylbenzene.<sup>44</sup>

Practically, no other products except cymenes and *n*-propyltoluenes were observed under our reaction conditions. As a result, *iso/n*-propyltoluene ratio increases substantially in the sequence: conventional MFI < nanosheet MFI layered (mesostructured) zeolites. Although hexagonally mesostructured 10-ring zeolite exhibits higher cymene selectivity than both disordered 10-ring zeolites, it produces about 3% *n*-propyltoluenes resulting in a lower *iso/n*-propyltoluene (Fig. 7).

Most interestingly, *para*-selectivities of these zeolites differ substantially. Thermodynamically, *p*-cymene should be formed at about 30%, which is consistent with both disordered 10-ring zeolites. Slightly higher *para*-selectivity (35–38%) was obtained over hexagonally mesostructured 10-ring zeolite, which indicates some diffusional limitations in this structure compared to the other two zeolite catalysts. Conventional MFI zeolite exhibited the highest selectivity to *p*-cymene reaching 80% after 180 min of time-on-stream. Selectivity to *p*-cymene over MFI nanosheets formed from two pentasil layers increases from almost 50 to 58% after 180 min of T-O-S. This evidences that the alkylation and transalkylation reactions proceed to a

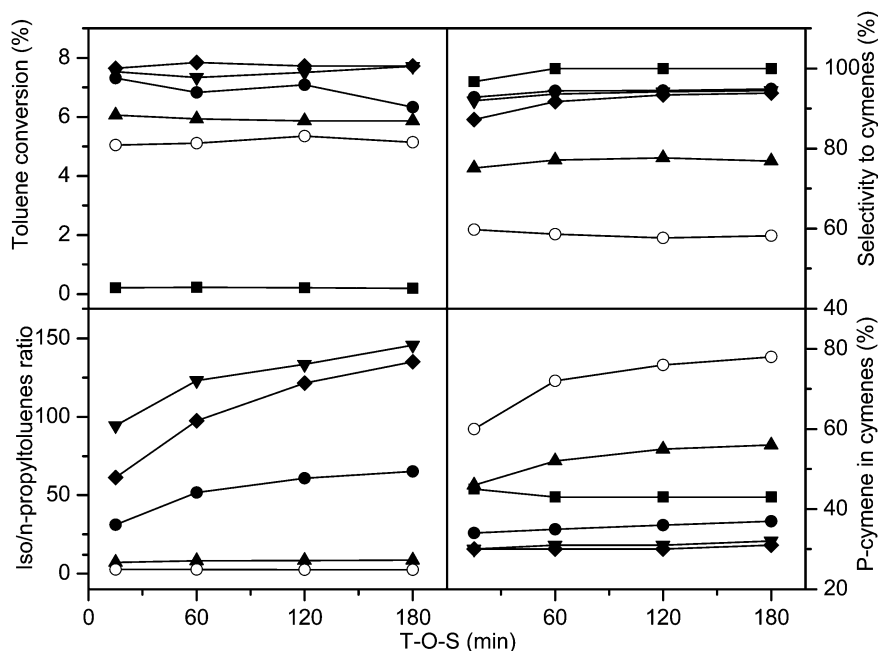


Fig. 7 Toluene alkylation with isopropyl alcohol over different nanostructured zeolite catalysts at 250 °C (● N<sub>3</sub>-5d, ▲ N<sub>3</sub>-9d, ▼ N<sub>4</sub>-5d, ◆ N<sub>5</sub>-5d, ○ MFI, ■ N<sub>3</sub>-1d).

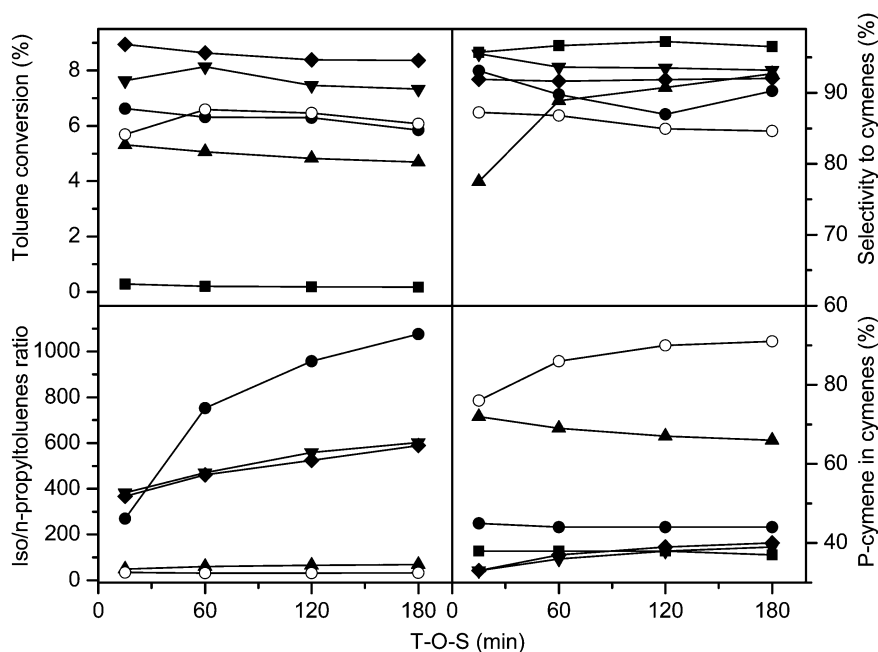


Fig. 8 Toluene alkylation with isopropyl alcohol over different nanostructured zeolite catalysts at 200 °C (● N<sub>3</sub>-5d, ▲ N<sub>3</sub>-9d, ▼ N<sub>4</sub>-5d, ◆ N<sub>5</sub>-5d, ○ MFI, ■ N<sub>3</sub>-1d).

large extent in the reaction volume between the two layers as diffusion limitations are in charge of the increased *para*-selectivity. The increase in *para*-selectivity over MFI nanosheet zeolite goes in parallel with the increase in *iso/n*-propyltoluene ratio. Similarly high *iso/n*-propyltoluene ratios were recently reported for extra-large pore zeolite UTL under the same reaction conditions<sup>45</sup> in contrast to MOR catalyst.<sup>46</sup>

Similar trends as for conversion and selectivities over zeolites under study were observed also at the reaction temperature

200 °C (Fig. 8). Toluene conversion, the level of which is governed by the rate of desorption and product transport is practically unchanged. As for the selectivities to individual products, they are rather comparable with those found at the reaction temperature 250 °C. Higher cymene selectivities at 200 °C can be related to the thermodynamic equilibrium, as the stability of *n*-propyl chains increases with increasing reaction temperature.

From the acidity point of view, it looks that the dominating factor for higher conversion of toluene in its alkylation with

isopropyl alcohol is the concentration of acid sites on the external surface. All three mesostructured catalysts exhibit substantially higher acid site concentration resulting in higher toluene conversion in contrast to lamellar and conventional MFI. High concentrations of *n*-propyltoluenes formed over lamellar and conventional MFI samples evidence that the alkylation reaction proceeds mainly in the channel system of MFI samples being followed by bimolecular formation of *n*-propyltoluenes.

## 4. Conclusions

Lamellar and mesostructured, probably 10-ring, zeolites were synthesized using specially designed templates preventing the crystallization in the third dimension. This synthetic approach enables to prepare ordered lamellar and mesostructured zeolites with a defined number of layers.

X-ray powder diffraction, transmission electron microscopy and adsorption isotherms provided clear evidence of the structure, morphology, and textural properties of these materials.

Characterization of the acidic properties of lamellar or mesostructured zeolites studied showed the presence of high concentrations of Lewis acid sites, which is probably due to a limited thickness of the lamellas in contrast to conventional MFI zeolite.

Conventional MFI zeolite was the most active in toluene disproportionation under different reaction conditions. Selectivities to *p*-xylene were not substantially changed by the textural properties of zeolites studied (novel zeolites *vs.* conventional one).

Lamellar and mesostructured zeolites were more active in toluene alkylation with isopropyl alcohol with respect to conventional MFI zeolite. Lamellar MFI zeolite consisting of two layers exhibited rather high *para*-selectivity as well as low *iso*/*n*-propyl ratio in cymene products. This is a clear consequence of the fact that the reaction proceeds inside the channel system and not on the external surface. Even two-layers of MFI zeolite can substantially enhance the *para*-selectivity in the formation of *p*-cymene in contrast to *p*-xylene.

## Acknowledgements

R.R. acknowledges the funding by the Research Center Program (CA1201) of IBS (Institute for Basic Science). N.Ž. and J.Č. acknowledge the Czech Science Foundation (P106/12/0189).

## References

- 1 A. Corma, *Chem. Rev.*, 1995, **95**, 559.
- 2 H. Jin, M. B. Ansari and S.-E. Park, *Adv. Porous Mater.*, 2013, **1**, 72.
- 3 J. Čejka, G. Centi, J. Perez-Pariente and W. J. Roth, *Catal. Today*, 2012, **179**, 2–15.
- 4 G. Bellussi, A. Carati, C. Rizzo and R. Millini, *Catal. Sci. Technol.*, 2013, **3**, 833.
- 5 K. B. Yoon, *Acc. Chem. Res.*, 2007, **40**, 29–40.
- 6 D. P. Serrano, J. M. Escola and P. Pizarro, *Chem. Soc. Rev.*, 2013, **42**, 4004.
- 7 M. Bejblová, D. Procházková and J. Čejka, *ChemSusChem*, 2009, **2**, 486.
- 8 R. E. Morris, *Top. Catal.*, 2010, **53**, 1291.
- 9 G. Centi and S. Perathoner, in *Zeolites and Catalysis: Synthesis, Reactions and Applications*, ed. J. Čejka, A. Corma and S. I. Zones, Wiley-VCH, Weinheim, 2010, ch. 24, vol. 2, p. 745.
- 10 J. Perez-Ramirez, C. H. Christensen, K. Egeblad, C. H. Christensen and J. C. Groen, *Chem. Soc. Rev.*, 2008, **37**, 2530.
- 11 J. Čejka, H. van Bekkum, A. Corma and F. Schüth, *Introduction to Zeolite Science and Practice, 3rd revised edition*, *Stud. Surf. Sci. Catal.*, Elsevier Science: Amsterdam, 2007, vol. 168.
- 12 W. J. Roth, C. T. Kresge, J. C. Vartuli, M. E. Leonowicz, A. S. Fung and S. B. McCullen, *Stud. Surf. Sci. Catal.*, 1995, **94**, 301.
- 13 A. Corma, V. Fornes, S. B. Pergher, Th. L. M. Maesen and J. G. Buglass, *Nature*, 1998, **396**, 353.
- 14 K. Na, C. Jo, J. Kim, K. Cho, J. Jung, Y. Seo, R. J. Messinger, B. F. Chmelka and R. Ryoo, *Science*, 2011, **333**, 328.
- 15 W. J. Roth, P. Chlubná, M. Kubů and D. Vitvarová, *Catal. Today*, 2013, **204**, 8.
- 16 W. J. Roth and J. Čejka, *Catal. Sci. Technol.*, 2011, **1**, 43.
- 17 W. J. Roth, *Stud. Surf. Sci. Catal.*, 2007, **168**, 221.
- 18 F. S. O. Ramos, M. K. de Pietre and H. O. Pastore, *RSC Adv.*, 2013, **3**, 2084.
- 19 K. Na, W. Park, Y. Seo and R. Ryoo, *Chem. Mater.*, 2011, **23**, 1273.
- 20 J. Kim, W. Park and R. Ryoo, *ACS Catal.*, 2011, **1**, 337.
- 21 W. Park, D. Yu, K. Na, K. E. Jelfs, B. Slater, Y. Sakamoto and R. Ryoo, *Chem. Mater.*, 2011, **23**, 5131.
- 22 E. Verheyen, C. Jo, M. Kurttepele, G. Vanbutsele, E. Gobechiya, T. I. Korányi, S. Bals, G. Van Tendeloo, R. Ryoo, C. E. A. Kirschhock and J. A. Martens, *J. Catal.*, 2013, **300**, 70.
- 23 P. Wu, J. Ruan, L. Wang, L. Wu, Y. Wang, Y. Liu, W. Fan, M. He, O. Terasaki and T. Tatsumi, *J. Am. Chem. Soc.*, 2008, **130**, 8178.
- 24 W. J. Roth, O. V. Shvets, M. Shamzhy, P. Chlubná, M. Kubů, P. Nachtigall and J. Čejka, *J. Am. Chem. Soc.*, 2011, **133**, 6130.
- 25 H. Xu, B. Yang, J.-G. Jiang, L. Jia, M. He and P. Wu, *Microporous Mesoporous Mater.*, 2013, **169**, 88.
- 26 L. Grajciar, O. Bludsky, W. J. Roth and P. Nachtigall, *Catal. Today*, 2013, **204**, 15.
- 27 K. Cho, K. Na, J. Kim, O. Terasaki and R. Ryoo, *Chem. Mater.*, 2012, **24**, 2733.
- 28 W. J. Roth, P. Nachtigall, R. E. Morris, P. S. Wheatley, V. R. Seymour, S. E. Ashbrook, P. Chlubná, L. Grajciar, M. Položij, A. Zukaal, O. V. Shvets and J. Čejka, *Nat. Chem.*, DOI: 10.1038/NCHEM.1662.
- 29 M. A. Climent, A. Corma and A. Velty, *Appl. Catal.*, A, 2004, **263**, 155.
- 30 A. Corma, V. Fornes, J. M. Guil, S. Pergher, Th. L. M. Maesen and J. G. Buglass, *Microporous Mesoporous Mater.*, 2000, **38**, 301.
- 31 A. Corma, U. Diaz, V. Fornes, J. L. Jorda and F. Rey, *Chem. Commun.*, 1999, 779.

- 32 A. Corma, U. Diaz, M. E. Domine and V. Fornes, *Chem. Commun.*, 2000, 137.
- 33 A. Corma, V. Fornes, J. L. Jorda, F. Rey, R. Fernandez-Lafuente, J. M. Guisan and C. Mateo, *Chem. Commun.*, 2001, 419.
- 34 J. Jung, C. Jo, K. Cho and R. Ryoo, *J. Mater. Chem.*, 2012, 22, 4637.
- 35 A. Corma, V. Fornés, L. Forni, F. Márquez, J. Martínez-Triguero and D. Moscotti, *J. Catal.*, 1998, 179, 451.
- 36 N. Y. Chen, W. W. Kaeding and F. G. Dwyer, *J. Am. Chem. Soc.*, 1979, 101, 6783.
- 37 N. Y. Chen and W. E. Garwood, *Catal. Rev. Sci. Eng.*, 1986, 28, 185.
- 38 B. Wichterlová and J. Čejka, *J. Catal.*, 1994, 136, 523.
- 39 J. Čejka and B. Wichterlová, *Catal. Rev.*, 2002, 44, 375.
- 40 C. Perego and P. Ingallina, *Green Chem.*, 2004, 6, 274.
- 41 B. Wichterlová, N. Žilková and J. Čejka, *Microporous Mater.*, 1996, 6, 405.
- 42 N. Žilková, M. Bejblová, B. Gil, S. I. Zones, A. W. Burton, C.-Y. Chen, Z. Musilová-Pavlačková, G. Košová and J. Čejka, *J. Catal.*, 2009, 266, 79.
- 43 I. I. Ivanova, D. Brunel, J. B. Nagy and E. G. Derouane, *J. Mol. Catal. A: Chem.*, 1995, 95, 243.
- 44 W. Kim, J.-C. Kim, J. Kim, Y. Seo and R. Ryoo, *ACS Catal.*, 2013, 3, 192.
- 45 N. Žilková, M. Shamzhy, O. V. Shvets and J. Čejka, *Catal. Today*, 2013, 204, 22.
- 46 T. Odedairo and S. Al-Khattaf, *Catal. Today*, 2013, 204, 73.